



## 3D imaging of subducting and fragmenting Indian continental lithosphere beneath southern and central Tibet using body-wave finite-frequency tomography



Xiaofeng Liang<sup>a,\*</sup>, Yun Chen<sup>a</sup>, Xiaobo Tian<sup>a,b</sup>, Yongshun John Chen<sup>c</sup>, James Ni<sup>d</sup>, Andrea Gallegos<sup>d</sup>, Simon L. Klemperer<sup>e</sup>, Minling Wang<sup>f</sup>, Tao Xu<sup>a,b</sup>, Changqing Sun<sup>g</sup>, Shaokun Si<sup>h</sup>, Haiqiang Lan<sup>a</sup>, Jiwen Teng<sup>a</sup>

<sup>a</sup> State Key Laboratory of Lithospheric Evolution, Institute of Geology and Geophysics, Chinese Academy of Sciences, Chaoyang, Beijing 100029, China

<sup>b</sup> CAS Center for Excellence in Tibetan Plateau Earth Sciences, Beijing, 100101, China

<sup>c</sup> Institute of Theoretical and Applied Geophysics, School of Earth and Space Sciences, Peking University, 100871, China

<sup>d</sup> Department of Physics, New Mexico State University, Las Cruces, NM 88003, USA

<sup>e</sup> Department of Geophysics, Stanford University, Stanford, CA 94305, USA

<sup>f</sup> College of Earth Sciences, Guilin University of Technology, Guilin 541004, China

<sup>g</sup> Key Laboratory of Crustal Dynamics, Institute of Crustal Dynamics, China Earthquake Administration, Beijing, 100085, China

<sup>h</sup> Department of Investigation, National Deep Sea Center, State Oceanic Administration, Qingdao, 266061, China

### ARTICLE INFO

#### Article history:

Received 27 November 2015

Received in revised form 8 March 2016

Accepted 12 March 2016

Available online xxx

Editor: P. Shearer

#### Keywords:

Indian continental lithosphere  
Tibetan plateau  
bodywave traveltome tomography  
subduction  
fragmentation  
upper mantle

### ABSTRACT

We perform a finite-frequency tomographic inversion to image 3D velocity structures beneath southern and central Tibet using teleseismic body-wave data recorded by the TIBET-31N passive seismic array as well as waveforms from previous temporary seismic arrays. High-velocity bodies dip  $\sim 40^\circ$  northward beneath the Himalaya and the Lhasa Terrane. We interpret these high-velocity anomalies as subducting Indian Continental Lithosphere (ICL). The ICL appears to extend further north in central Tibet than in eastern Tibet, reaching 350 km depth at  $\sim 31^\circ\text{N}$  along  $85^\circ\text{E}$  but at  $\sim 30^\circ\text{N}$  along  $91^\circ\text{E}$ . Low P- and S-wave velocity anomalies extend from the lower crust to  $\geq 180$  km depth beneath the Tangra Yum Co Rift, Yadong–Gulu Rift, and the Cona Rift, suggesting that rifting in southern Tibet may involve the entire lithosphere. The anomaly beneath Tangra Yum Co Rift extends down to about 180 km, whereas the anomalies west of the Yadong–Gulu Rift and east of the Cona Rift extend to more than 300 km depth. The low-velocity upper mantle west of the Yadong–Gulu Rift extends furthest north and appears to connect with the extensive upper-mantle low-velocity region beneath central Tibet. Thus the northward-subducting Indian Plate is fragmented along north–south breaks that permit or induce asthenospheric upwellings indistinguishable from the upper mantle of northern Tibet.

© 2016 Elsevier B.V. All rights reserved.

### 1. Introduction

Four distinct models for the accommodation of convergence between the Indian and Eurasian continents are: 1) underthrusting of Indian lithosphere (e.g., Argand, 1924; Ni and Barazangi, 1984), 2) crustal injection and mantle–lithosphere subduction (e.g., Zhao and Morgan, 1987), 3) uniform viscous thickening of the Tibetan crust (e.g., Dewey and Burke, 1973; England and Houseman, 1986), and 4) convective removal of thickened mantle lithosphere and asso-

ciated plateau uplift (e.g., Molnar et al., 1993). The underthrusting model posits that the Indian lithosphere slides directly beneath the Tibetan crust, without an intervening Asian asthenospheric wedge. The crustal-injection model predicts a significant asthenospheric wedge between the subducting Indian mantle lithosphere and the Tibetan lithosphere. The viscous-thickening model assumes that the thickened Tibetan lithosphere is due to accordion thickening of the Indian and Asian lithospheres south and north of the Indus–Yarlung Suture (IYS). Finally, the convective-removal model attempts to explain the rather uniform uplift of the entire Tibetan Plateau by attributing it to the loss of a continental lithospheric root after earlier thickening.

Over the last two decades a large number of temporary seismic arrays have been operated across the Himalayas and most of Tibet. Many geophysical observations have suggested that the Indian

\* Corresponding author at: Institute of Geology and Geophysics, Chinese Academy of Sciences, 19 Beitucheng West Road, Chaoyang, Beijing, 100029, China. Tel.: +86 10 82998331.

E-mail address: liangxf@mail.iggcas.ac.cn (X. Liang).

Continental Lithosphere (ICL) underthrusts southern Tibet south of the Bangong-Nujiang Suture (BNS), including observations of high Pn velocity and low Sn attenuation (e.g., Ni and Barazangi, 1983; McNamara et al., 1995), a doublet of converted Ps phases in the lower crust and at the Moho (e.g., Owens and Zandt, 1997; Kind et al., 2002; Schulte-Pelkum et al., 2005; Nabelek et al., 2009; Zhao et al., 2010; Zhang et al., 2014a, 2014b), shear-wave splitting features (e.g., Huang et al., 2000; Fu et al., 2008; Chen et al., 2010a; Zhao et al., 2014), fast surface-wave velocity anomalies (e.g., Priestley et al., 2008; Acton et al., 2010; Chen et al., 2010b; Fu et al., 2010; Jiang et al., 2011; Ceylan et al., 2012; Agius and Lebedev, 2013), fast body-wave velocity anomalies (e.g., Tilmann et al., 2003; Li et al., 2008; He et al., 2010; Hung et al., 2011; Liang et al., 2012; Zhang et al., 2015), and gravity anomalies (Jin et al., 1996). However, due to non-uniform seismic station coverage and the imprecision of existing tomographic images of the Indian and Tibetan lithosphere beneath Tibet, the geometry, northern extent and lateral continuity of the Indian lithosphere have been much debated.

Significant east–west lateral variations in the geometry and the thickness of the ICL have been inferred in recent studies. Zhou and Murphy (2005) proposed a wholesale underthrusting of ICL with a weakened zone between 84°–92°E. Liang and Song (2006) found a broad N–S zone of low Pn velocity (~8.0 km/s) along 89°–90°E. From the eastern Himalayan syntaxis to the Karakoram Fault, according to Li et al. (2008), the Indian lithosphere underthrusts Tibet at an increasingly shallow angle and reaches progressively further to the north (Fig. 1). However, other regional tomographic images show high velocities extending further north toward the Jinsha Suture (JS) in the easternmost part of the plateau (Liang et al., 2012; Nunn et al., 2014). Bao et al. (2015) suggested that the ICL is underthrusting horizontally under the western and eastern Tibetan Plateau, but it is steeply subducting under the central plateau. Furthermore, receiver-function images (e.g., Kumar et al., 2006; Zhao et al., 2010) as well as body- and surface-wave tomographic models (e.g., Li et al., 2008; Ren and Shen, 2008; He et al., 2010; Liang et al., 2011; Ceylan et al., 2012; Nunn et al., 2014) suggest significant east–west lateral variations in the dipping geometry of the ICL.

In a similar fashion, west–east lateral variations at the surface of the plateau are well known, particularly the north–south trending rifts of southern Tibet (e.g., Molnar and Tapponnier, 1978; Ni and York, 1978; Armijo et al., 1986). Minor N–S diking and associated east–west extension initiated by 19 Ma (Mitsuishi et al., 2012), resulting in the north–south trending extensional grabens that remain active today (Fig. 1, from west to east, Tangra Yum Co Rift (TYR), Punqu Xianza Rift (PXR), Yadong Gulu Rift (YGR), and Cona Rift (CR)). These rifts are a manifestation of east–west extension of southern Tibet, roughly perpendicular to the India–Eurasia convergence direction. Whether these rifts are restricted to the upper crust or whether they involve the entire lithosphere is still debated (e.g., Masek et al., 1994; Yin, 2000; Tian et al., 2015). Crustal-scale mechanisms proposed to explain the rifting process include lower-crustal east–west flow (e.g., Molnar et al., 1981; Royden et al., 1997), oblique convergence or basal shear associated with the underthrusting ICL (e.g., McCaffrey and Nabelek, 1998), and inherited architectures (Faizabad and Munger-Saharsa basement ridges, Fig. 1) in the underthrust Indian crust (e.g., Godin and Harris, 2014). Lithospheric-scale processes have also been invoked, including gravitational collapse following the attainment of maximum elevation (e.g., Molnar and Tapponnier, 1978; Liu and Yang, 2003), deformation facilitated by mantle–lithosphere delamination (Ren and Shen, 2008), and fragmentation of the ICL (e.g., Yin, 2000; Liang et al., 2012; Chen et al., 2015).

Liang et al. (2012) discussed the geometry of the ICL and its west–east variation, but that paper mainly focused on eastern Ti-

bet based on the data coverage provided by the ASCENT project. In this paper we add data from the TIBET-31N, a 600-km-long west–east passive-source linear seismic array that ranges from Cuoqin to Nam Tso and was operated by the Institute of Geology and Geophysics, Chinese Academy of Sciences from September 2009 to November 2010 (Chen et al., 2015). Our 48 temporary seismographs were equipped with Guralp CMG-3ESP sensors and Reftek-72A/130 data loggers. We also recorded a 10-station profile across the northern YGR (Zhang et al., 2013) (Fig. 1). We include all other currently available seismic data to provide a body-wave travel-time tomography model that is clearly improved over earlier work (Figs. S1 and S2). We use our new model to address the west–east variations of upper-mantle structures in southern and central Tibet.

## 2. Data

Linear seismic arrays provide 2D images that can be used to understand the collision process that formed the high plateau but they do not provide a complete picture of the 3D structure of the crust and mantle. By combining the data from several 2D arrays to provide broad lateral coverage, 3D teleseismic tomography images can illuminate the upper-mantle structures of southern Tibet. In this study we combine data from eight temporary seismic arrays deployed over the past twenty years in central and southern Tibet: INDEPTH II (12 stations, Kosarev et al., 1999) and III (42 stations, Huang et al., 2000), BHUTAN (5 stations, Velasco et al., 2007), Namche Barwa (69 stations, Sol et al., 2007), Hi-CLIMB (218 stations, Nabelek et al., 2009), HIMNT (28 stations, Schulte-Pelkum et al., 2005), RISE (13 stations, Jin et al., 2009) and TIBET-31N (57 stations, Chen et al., 2015), as well as the Global Seismic Network Lhasa station (LSA) for a combined dataset of 445 stations (Fig. 1). The resolution of the body-wave tomography for upper mantle structures beneath the Lhasa Terrane is dramatically improved by including our TIBET-31N stations (Figs. S1 and S2).

We selected earthquakes for which direct P (or S) were recorded by at least 4 stations from epicentral distances of 30–90° (to minimize interference from the mantle transition zone and core–mantle boundary). PcP and ScS phases with shorter epicentral distances were also identified to improve the data coverage (Fig. 1, inset). Because our dataset spans nearly 20 yrs of campaign data operated at different epochs, we use the permanent GSN station LSA as a common reference when measuring differential travel times to make inter-network measurements possible. Because different frequencies sample different spatial regions along the ray paths (e.g., Dahlen et al., 2000), two different frequency bands of waveform data were extracted separately for P- and S-waves in order to apply a finite-frequency travel-time tomography algorithm. We measured the arrival times of P and S phases in high and low-frequency bands (0.5–2 Hz and 0.1–0.5 Hz for the P, 0.1–0.5 Hz and 0.05–0.1 Hz for the S), and obtained differential travel times using the AIMBAT software package (Lou et al., 2013) based on stacking-correlation (Pavlis and Vernon, 2010) and multi-channel cross-correlation (MCCC) (VanDecar and Crosson, 1990). We used 109 002 high-frequency and 34 637 low-frequency P-wave travel times and 23 614 high-frequency and 20 956 low-frequency S-wave travel times in our inversions. Lateral P- and S-wave velocity variations are directly indicated by azimuthally averaged differential travel times at each station along the TIBET-31N profile (Fig. 2a and b). These differential travel times already show a first-order feature of our final model: increased delays are seen at stations from 88–90°E, compared to stations further west and further east.

## 3. Method

We used finite-frequency seismic tomography to invert for P- and S-wave crustal and upper-mantle velocity structures beneath

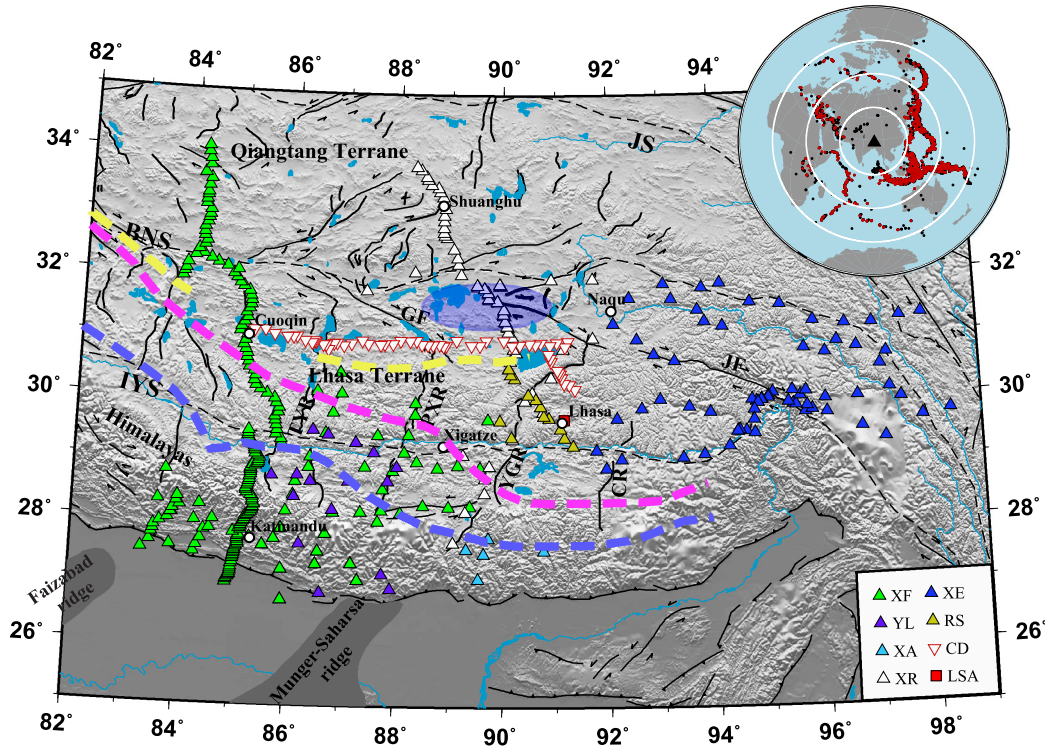


**Fig. 1.** Tectonic and topographic map of the south-central Tibetan Plateau and seismic stations used in this study (XF: Hi-CLIMB, XE: Namche Barwa, YL: HIMNT, XA: Bhutan, XR: INDEPTH II&III, RS: RISE, CD: TIBET-31N). Blue-shaded region: high-velocity anomaly from Tilmann et al. (2003) P-wave tomography. Blue, purple, and yellow lines: 100, 200, and 300 km depth contours on top of Indian lithosphere from Li et al. (2008) P-wave tomography. Structures from the HimaTibetMap dataset (Styron et al., 2010) include MFT: Main Frontal Thrust, IYS: Indus-Yarlung Suture, BNS: Bangong-Nujiang Suture, JS: Jinsha Suture, JF: Jiali strike-slip fault, GF: Gyring Co strike-slip fault, CR: Cona Rift, YGR: Yadong-Gulu Rift, PXR: Pumqu-Xianza Rift and TYR: Tangra Yum Co Rift. Grey-shaded areas on the Indian plate: Faizabad and Munger-Saharsa basement ridges (Godin and Harris, 2014). Upper-right inset shows events used in this study. Black and red dots show event locations for P- and S-wave event locations, respectively. (For interpretation of the references to color in this figure legend, the reader is referred to the web version of this article.)

south-central Tibet. The methodology has been thoroughly discussed and routinely used in previous works (e.g., Dahlen et al., 2000; Hung et al., 2011; Liang et al., 2011), so is not described in detail here. Since only differential travel times are used in the inversion, only lateral velocity contrasts can be resolved. We present all results as % differences in  $V_p$  and  $V_s$  from an average velocity in our model at each depth.

### 3.1. Model parameterization and inversion

We parameterized the volume beneath our study area ( $20^\circ$  in longitude,  $14^\circ$  in latitude, and 900 km in depth) with a regular  $65 \times 65 \times 33$  grid centered at  $90^\circ\text{E}$ ,  $29^\circ\text{N}$ . This model is large enough to include most of the differential travel-time sensitivity kernels in our model space, and has a cell spacing of  $\sim 0.31^\circ$  longitude,  $\sim 0.22^\circ$  latitude, and 28 km depth. Every cell has uniform velocity during the inversion. With this parameterization, travel time equations can be written as:

$$d_i = G_{il} m_l \quad (1)$$

where  $d_i$  is the  $i$ th differential travel time,  $G_{il}$  is the differential value of the integrated volumetric kernels of the  $i$ th event contributing to the  $l$ th node, and  $m_l$  is the model parameter at the  $l$ th node. We resolved the inversion problem using a standard damped least-squares method with smoothing:

$$\hat{m} = (G^T G + \theta^2 I + \eta D^T D)^{-1} G^T d \quad (2)$$

where  $I$  is the identity matrix and  $D$  are first-order Laplacian vectors. The damping parameter  $\theta$  is determined empirically by examining the data-variance reduction versus the L2 norm of inverted models represented by a trade-off curve (Fig. S3). We chose

the damping parameter that yields an optimum variance reduction and a relatively small model norm. Smoothing parameter  $\eta$  is also picked empirically to get a smoothly variable model. The model discussed in this paper used a damping and a smoothing parameter that yields a variance reduction of  $\sim 69\%$  for P phases and  $\sim 68\%$  for S phases. The mean value and standard deviation of the input travel times are 0.0038 and 0.4576 for P phases. In the case of S phases, the mean value and standard deviation of the input travel times are 0.0008 and 1.0004. After the inversion, the mean value and standard deviation of the travel times are changed to  $-0.0014$  and 0.2522 for P phases and  $-0.0023$  and 0.5642 for S phases (Fig. 3). And after the inversion, the final travel-time residuals in both the high- and low-frequency bands were much smaller when compared with the input differential travel times (Figs. 3, S4 and S5).

### 3.2. Crustal and elevation correction

The raypaths of teleseismic body waves are more vertical near the surface. Therefore shallow velocity structures are poorly constrained by our relative travel-time data. In teleseismic travel-time tomography crustal corrections are needed in order to reduce the tradeoff between crustal and mantle velocity heterogeneities. In order to correct for crustal effects, we calculated frequency-dependent crustal corrections for each event-station record from the synthetic crustal response of an incoming plane wave beneath that station (Yang and Shen, 2006). We tested several crustal models including CRUST2.0 (Bassin et al., 2000), SEAPS (Sun et al., 2004, 2008), and CRUST1.0 (Laske et al., 2013) (Figs. S6, S7, S8 and S9), but we did not find any major differences in large-scale features ( $>200$  km) (Liang et al., 2012). We used the crustal structure from SEAPS where available, because it is a body-wave derived

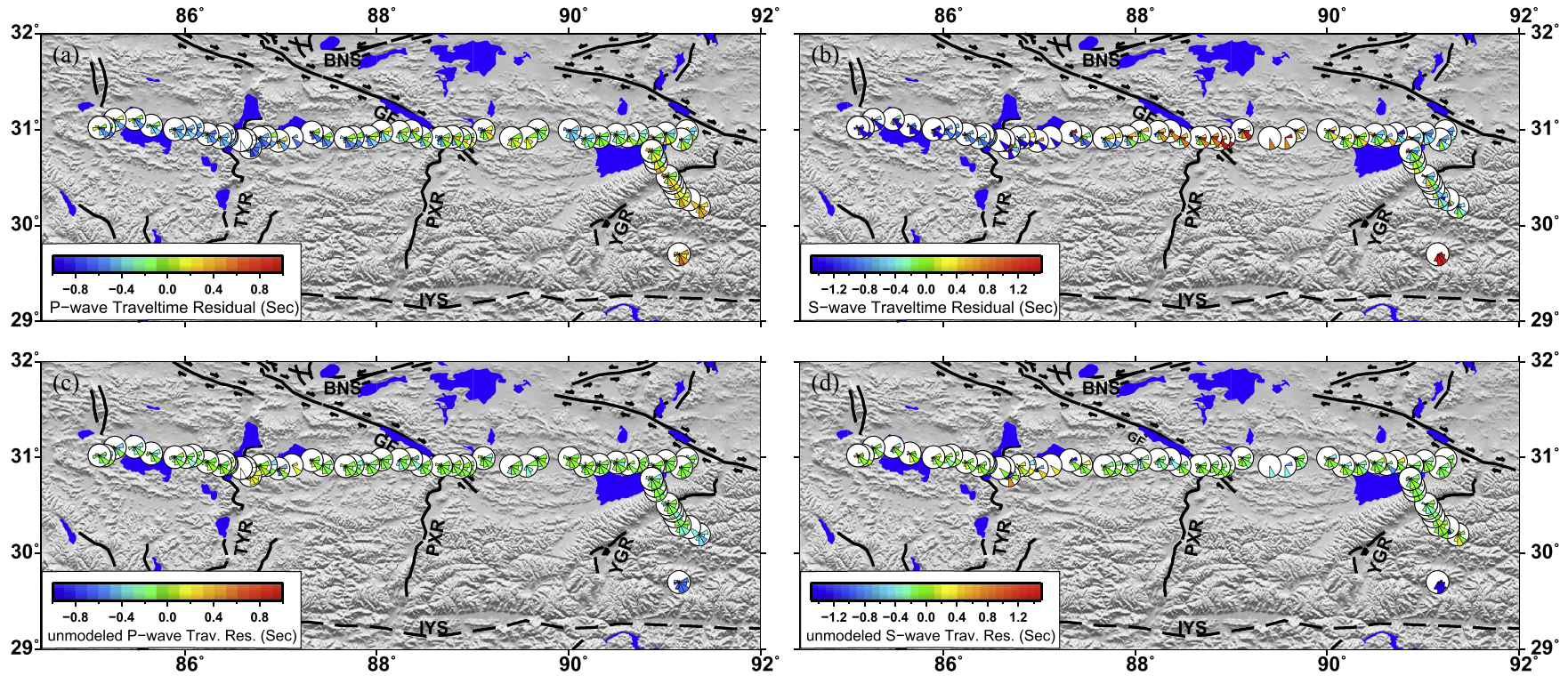


**Fig. 2.** Sector diagrams of azimuthally averaged differential travel times for TIBET-31N, for P (a and c) and S (b and d), before (a and b) and after (c and d) the tomographic inversion, respectively. Travel-time residuals before the inversion represent the differential travel times from MCCC measurements. Travel-time residuals after the tomographic inversion represent the difference between the measured differential travel times and the synthetic travel times calculated based on inverted  $V_p$  and  $V_s$  models. Sector lengths show normalized measurements in a  $30^\circ$  back-azimuth range at each station. The color of each  $30^\circ$  back-azimuth is based on the averaged travel-time residuals in this back-azimuth range. Because of the large number of data, the averaged travel-time residuals reflect the general travel-time residual values in that back-azimuth range. These travel-time residuals average different ray-paths with similar back-azimuths that have sampled similar regions beneath our study area. (For interpretation of the references to color in this figure legend, the reader is referred to the web version of this article.)

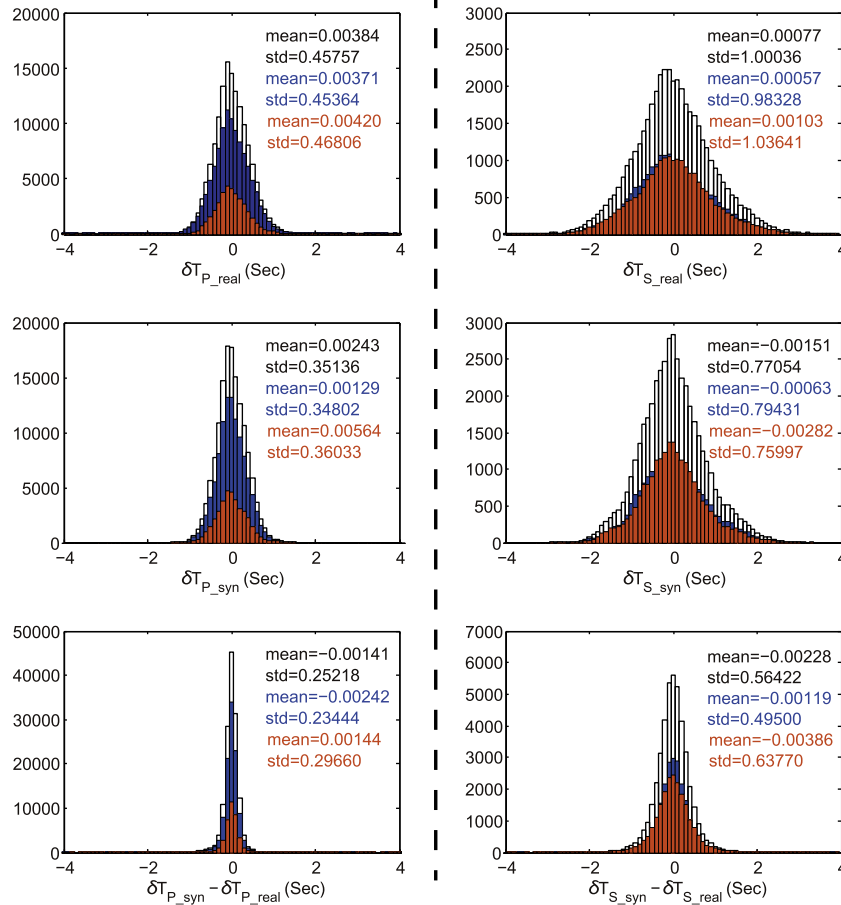


**Fig. 3.** Histograms of differential travel times from MCCC measurements ( $\delta T_{P\_real}$ ,  $\delta T_{S\_real}$ ), synthetic travel times from final tomographic models ( $\delta T_{P\_syn}$ ,  $\delta T_{S\_syn}$ ) and their differences ( $\delta T_{P\_syn} - \delta T_{P\_real}$ ,  $\delta T_{S\_syn} - \delta T_{S\_real}$ ) for both P- and S-waves. The black bars show the histogram of both high- and low-frequency data, blue bars show the histogram of high-frequency data, and red bars show the histogram of low-frequency data. The mean values and standard deviations of the different data group are shown using the same color as the bars. The width of each bar is 0.1 s. (For interpretation of the references to color in this figure legend, the reader is referred to the web version of this article.)

model and should therefore be more comparable with our results. For the few stations where SEAPS is not defined we used CRUST2.0 (Fig. S6). To minimize the influence of poor crustal-structure resolution we did not include the kernels of the top 50 km in the inversion. Instead we used crustal corrections and an additional free term for each station, which was incorporated into the inversion to absorb travel-time shifts caused by remaining shallow velocity heterogeneities (Fig. S10). We also tested the effect of pushing the travel-time anomalies into shallow depths by using a smaller damping factor for the top three layers of the model grids in the inversion. When we performed this test we could not see a significant difference between the upper mantle images (Figs. S11 and S12). These tests demonstrated our final models should not be significantly influenced by unmodeled shallow structures.

### 3.3. Resolution tests

3D resolution tests were performed to evaluate the data coverage and the ability of the inversion to recover upper-mantle structures (Figs. 4 and 5). Synthetic travel times were computed by multiplying the G-matrix with different input velocity models:  $\Delta t_{syn} = G \cdot \Delta c_{syn} + t_{noise}$ , where  $\Delta c_{syn}$  represents synthetic velocity perturbations,  $G$  is the differential value of the integrated volumetric kernels,  $\Delta t_{syn}$  represents the final synthetic travel-times, and  $t_{noise}$  represents Gaussian random noise with a standard deviation

of 0.1 s, which is about 10% of the typical differential travel-time span for a single event. Inversions were then performed using the same damping and smoothing parameters as those used in our inversion of the real data.

Checkerboard resolution tests were conducted using input anomalies with a diameter of 6 grid cells ( $\sim 170$  km) in all three dimensions (Fig. 4). The maximum input velocity perturbation of our checkerboards is  $\pm 2\%$  for the P-wave and  $\pm 4\%$  for the S-wave. The magnitude decreases from the center of each checkerboard cell to zero at the boundary as a cosine function. Our checkerboard resolution tests show that input anomalies are recovered reasonably well in regions with good ray coverage. However, anomaly intensities are strongly damped during the inversion to about 1/3 to 1/2 of the input anomaly intensity, so we do not discuss absolute anomaly amplitudes in this paper.

In addition to the checkerboard tests we carried out custom resolution tests to demonstrate our ability to recover two distinct features of our final tomographic images which become important to our later interpretations, namely the northward dipping high-velocity zone and an overlying low-velocity region (Fig. 5). We also carried out a series of resolution tests of the high-velocity zone using different depths to understand the degree of vertical smearing. For both P- and S-waves, the north-dipping high-velocity zone is not a shallow anomaly and must extend to  $>350$  km depth (Figs. S13 and S14).

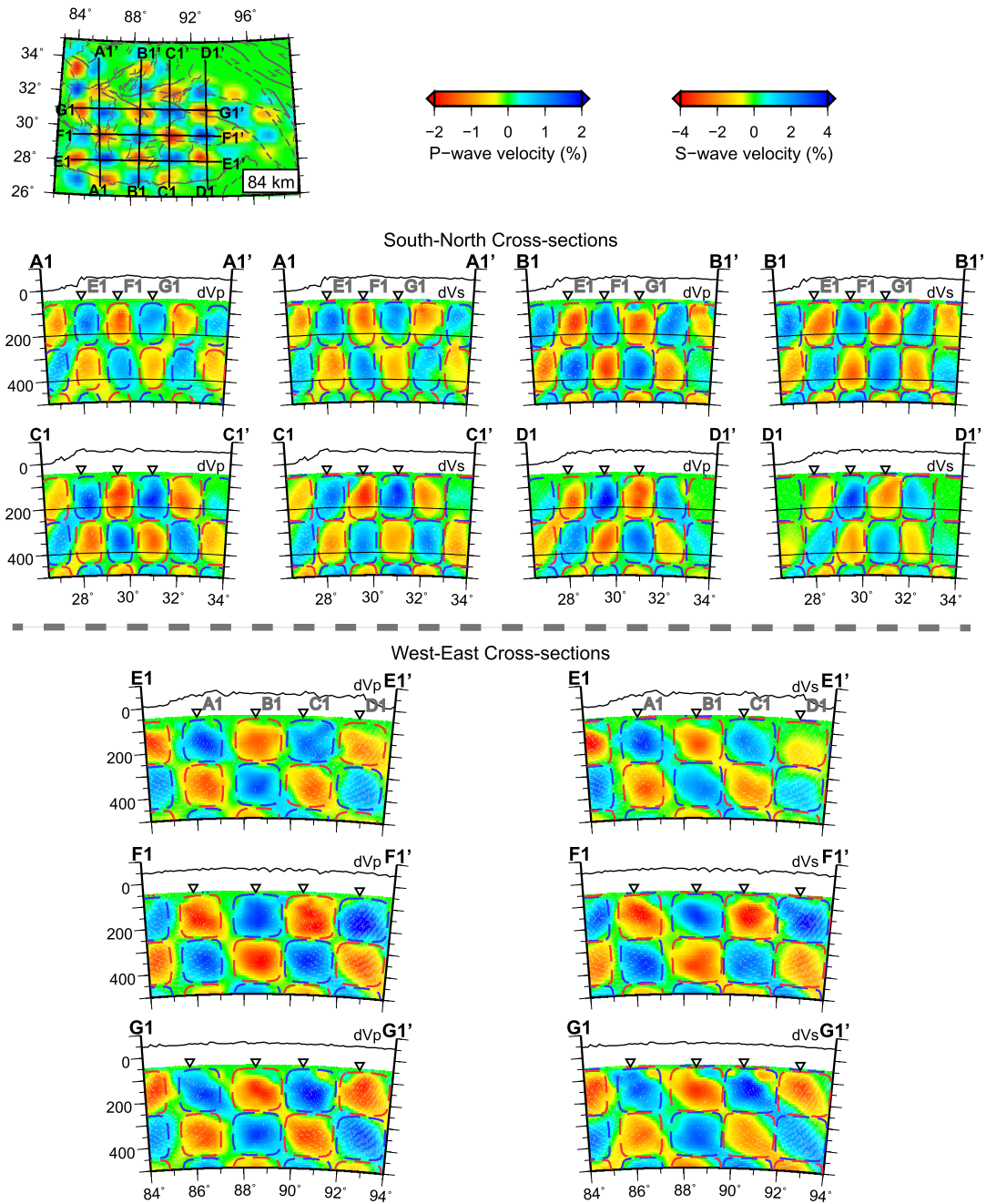


**Fig. 4.** Three-dimensional checkerboard test results using the same damping parameters as our final models. Checkers have a width (half-wavelength) of  $\sim 170$  km. Blue and red dashed lines overlain on the output images are  $\pm 2\%$  for the P-velocity ( $\pm 4\%$  for S-velocity) contours of the starting model. Open inverted triangles show the intersection points of south–north and west–east cross-sections. (For interpretation of the references to color in this figure legend, the reader is referred to the web version of this article.)

#### 4. Results

By combining all available travel-time data we obtain comprehensive 3D images of the upper mantle beneath southern and central Tibet (Figs. 6, 7 and 8) that provide new insights into the geometry of the ICL. A prominent high-velocity anomaly is observed along the Himalayas dipping  $\sim 40^\circ$  northward from  $\sim 80$ – $170$  km depth. We trace this anomaly from  $\sim 84^\circ$ E to  $92^\circ$ E, the full longitudinal range of our good data coverage. This high-velocity anomaly steepens from west to east, as it reaches 350-km depth at  $\sim 31^\circ$ N along  $85^\circ$ E (Fig. 7a, section A–A') but at  $\sim 30^\circ$ N along  $91^\circ$ E (section E–E'). There exists a lateral gap in the high-velocity structure at  $\sim 89^\circ$ E to  $90^\circ$ E (ICL shown in

Fig. 7a D–D', Fig. 7b F–F' and Fig. 8). We interpret this high-velocity body as subducting ICL following previous P-wave tomography results (Li et al., 2008) (Figs. 1 and S15). Based on the dip of this high-velocity anomaly, we use 'subduction' rather than 'underthrusting' to describe the geometry of the ICL. We also note a possible thinning of the subducting ICL in the down-dip direction at  $\sim 180$ – $220$  km depth (Fig. 7a, sections A–A', B–B').

A continuous low-velocity anomaly lies beneath the IYS in the uppermost mantle in both the P- and S-wave images (LV or LVBI: Low-Velocity Beneath the IYS, Figs. 6, 7, S16 and S17). This anomaly reaches only  $\sim 100$ – $150$  km depth beneath the TYR whereas it reaches up to  $\sim 300$  km around the YGR and the CR

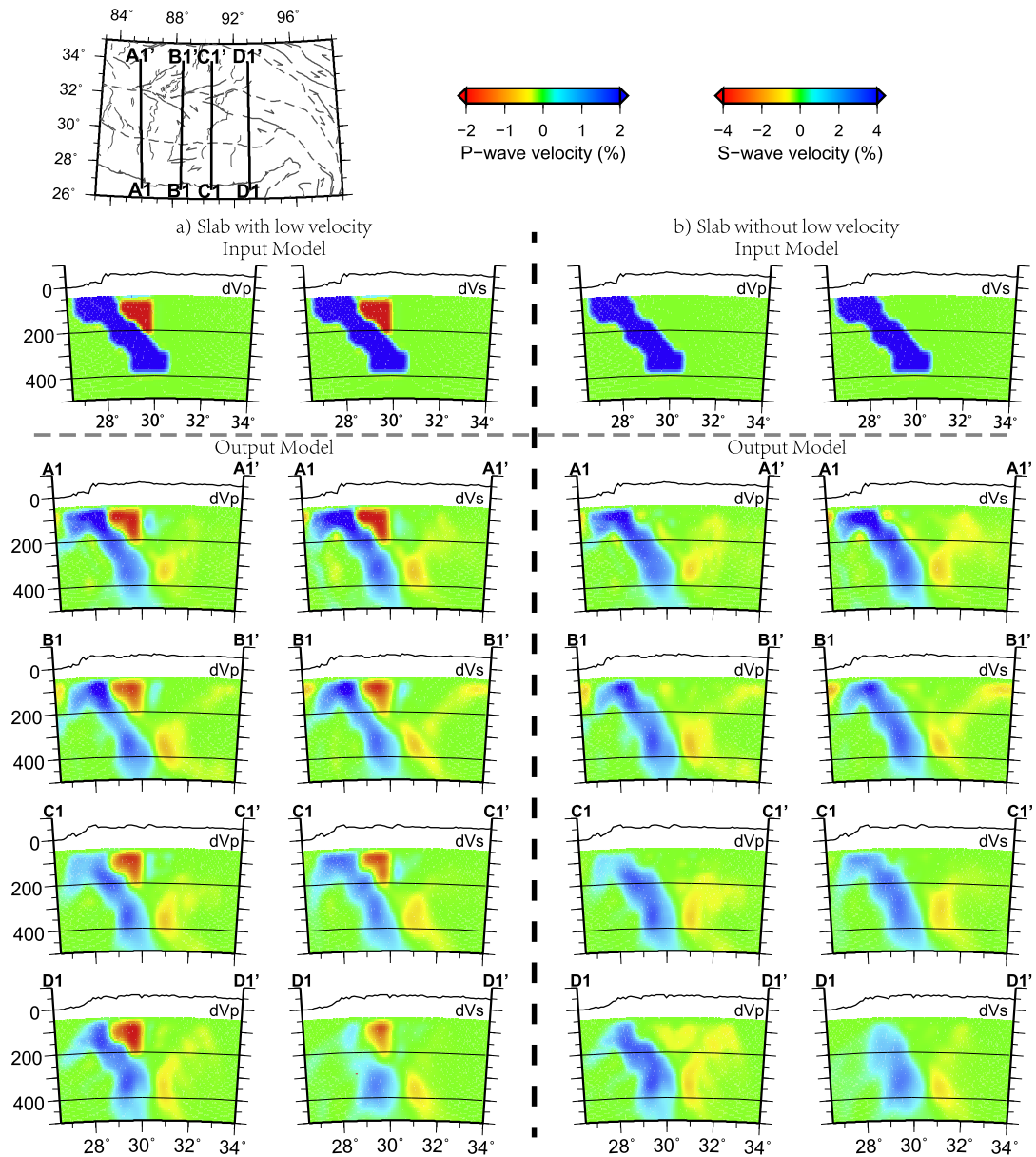


**Fig. 5.** P- and S-model recovery tests. (a) The input model has a high-velocity slab with a moderate subduction angle and an uppermost-mantle low-velocity anomaly. (b) The input model only has a high-velocity slab. The top panels show the input models. The inverted models demonstrate good recovery of both high- and low-velocity anomalies. (For interpretation of the references to color in this figure legend, the reader is referred to the web version of this article.)

(Fig. 7b, section G–G'). This feature has previously been interpreted as fragmentation of the ICL underneath southern Tibet (Liang et al., 2011, 2012) or alternatively as delamination of the ICL beneath eastern Tibet (Ren and Shen, 2008).

Beneath the northern Lhasa Terrane both our P- and S-wave images show consistently high velocities in the upper mantle (HV or HVBNL: High-Velocity Beneath Northern Lhasa terrane, Figs. 6, 7, 8, S16 and S17) except in the region close to 90°E (LVBYG: Low-Velocity Beneath the Yadong-Gulu Rift, D–D' in Fig. 7a, and Fig. S17), where there is significant low S-wave velocity and moderately low P-wave velocity. In the Qiangtang Terrane, north of the BNS, both the P- and S-wave images show strong low-velocity anomalies in the upper mantle (LVBNT: Low-Velocity Beneath the Northern Tibet, Fig. S14) albeit with relatively low resolution due to less data coverage on the northern edge of our study region. The low-velocity upper mantle beneath northern Tibet is in good agreement with prior body- and surface-wave tomography re-

sults (e.g., Wittlinger et al., 1996; Tilmann et al., 2003; Li et al., 2008; Chen et al., 2010b; Ceylan et al., 2012; Liang et al., 2012; Agius and Lebedev, 2013). As in these prior studies, we find it difficult to determine the depth extent of the low-velocity region.

The low-velocity anomaly close to 90°E (LVBYG) is connected to similar low-velocity bodies beneath the IYS and central-northern Tibet (D–D' in Fig. 7a, Fig. S17). This anomaly might indicate detachment of the Indian lithosphere (Ren and Shen, 2008) or it might represent a gap in the ICL that connects the shallower low-velocity body in southern Tibet (LVBI) to the much larger low-velocity regions in the upper mantle of central-northern Tibet (LVBNT). We note the correspondence of the LVBNL with a region of high-frequency Sn blockage (Ni and Barazangi, 1983; McNamara et al., 1995), whereas the LVBYG is aligned with the southernmost extent of the region of inefficient high-frequency Sn propagation (Barron and Priestley, 2009).

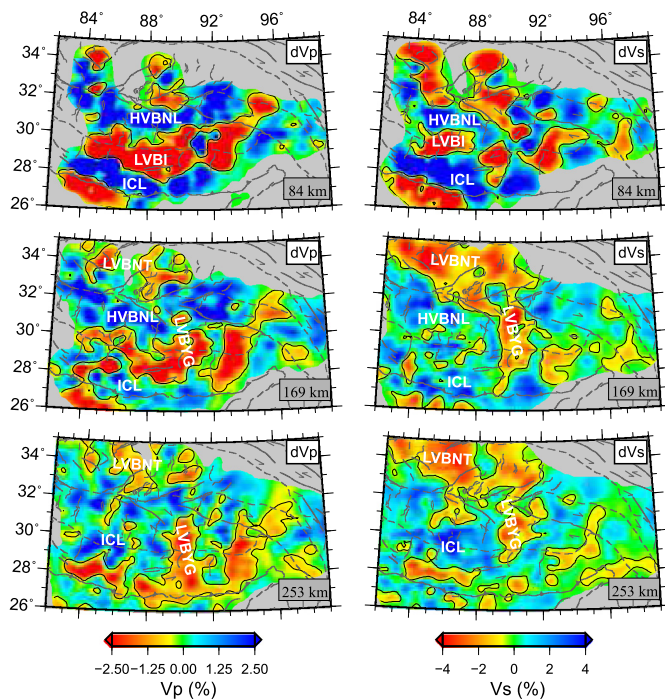


**Fig. 6.** Velocity structures beneath southern and eastern Tibet from our finite-frequency teleseismic travel-time tomography. Horizontal slices of P- and S-wave velocities are shown at depths of 84 km, 169 km, and 253 km. Vp and Vs images are clipped based on data coverage (the intensity for P- and S-wave travel-time sensitivity kernels, Figs. S1 and S2). The geological structures of Fig. 1 are shown as gray lines. ICL: Indian Continental Lithosphere; HV or HVBNL: High-Velocity anomalies Beneath the Northern Lhasa Terrane; LV or LVBI: Low-Velocity anomalies Beneath the IYS; LVBNT: Low-Velocity Beneath Northern Tibet. (For interpretation of the references to color in this figure legend, the reader is referred to the web version of this article.)

## 5. Discussions

### 5.1. Underthrusting, subduction, or detachment of Indian continental lithosphere?

At least three different possible geodynamic scenarios for accommodating convergence of India and Asia have been proposed: (1) horizontal underthrusting of the entire Indian lithosphere beneath Tibet as an integral body, (2) subduction of the Indian lithosphere at intermediate angles analogous to oceanic subduction (of either the entire ICL or only the Indian mantle lithosphere after delamination from all or part of the Indian continental lower crust), and (3) detachment (break-off) of a portion of Indian lithosphere followed by vertical sinking into the deeper mantle. All three may have been active at different times during orogenic evolution and all three may now characterize different locations beneath the Tibetan Plateau (e.g., DeCelles et al., 2002). Older seismic data from the Tibetan Plateau were widely interpreted to show a clear dichotomy in the uppermost mantle between faster wave speeds beneath southern Tibet and slower wave speeds beneath northern Tibet (e.g., Ni and Barazangi, 1983; McNamara et al., 1995). The seismically faster and presumably colder/stronger mantle beneath southern and central Tibet was widely interpreted as the ICL, underlying beneath the Tibetan crust.

More recent work has attempted to identify west–east variations in the northern limit of the ICL. Li et al. (2008) and Zhao et al. (2010) suggest the ICL extends further north to the west of 89°E, whereas Liang et al. (2012) found that the ICL extends further north to the east of 92°E. Nunn et al. (2014) followed Agius and Lebedev (2013) in suggesting horizontal underthrusting in cen-

tral Tibet (~88°E) as far north as the BNS with moderate-angle subduction occurring in eastern Tibet (~93°E). West–east differences in seismic velocity and the apparent northward extent of the ICL could correspond to an irregular northern boundary along which a portion of the ICL may have detached at an earlier time. They may also correspond to complex processes of active delamination or detachment or to velocity variations inherited from the Indian craton. Finally, ICL and Asian lithosphere may be more difficult to differentiate further north. Because we have included more data (Fig. 1) and so improved our resolution over previous models (Figs. S1 and S2), we feel confident about the existence of the P- and S-wave high-velocity body beneath southernmost Tibet that extends down to ~400 km depth with ~40° dip angle (ICL, Figs. 6, 7, 8), the high-velocity body beneath the northern Lhasa terrane (HV or HVBNL, Figs. 6, 7 and S17), and the low-velocity body at 100 km depth beneath the IYS (LV or LVBI, Figs. 6 and 7). Horizontal underthrusting of the coherent ICL directly beneath the present Tibetan crust seems precluded everywhere from 85°E (AA') to 91°E (F–F') by the existence of the LVBI that is seen beneath the IYS in all our south–north cross-sections. This is consistent with the inefficient propagation of high-frequency Sn, presumably due to a negative velocity gradient directly below the Moho as far south as the IYS (Barron and Priestley, 2009). The geometry and nature of the deeper high-velocity body (ICL) then determines our interpretation as to whether the ICL is better described as subducting or detaching body.

Our cross-sections A–A' and B–B' (Fig. 7a) show a continuous north-dipping ICL in a geometry strongly suggestive of subduction. Our tomography lacks the resolution within the crust to distinguish between subduction of the entire ICL or delamination and subduction only of the lower ICL, so we follow recent receiver-function interpretations of north-dipping converters in the upper mantle beneath southern Tibet as implying delamination of the Indian mantle lithosphere from the Indian lower crust (Kosarev et al., 1999; Shi et al., 2015). Delamination is also supported by numerical modeling that recognizes that if Indian upper crust is underthrust beneath Tibet, the remaining Indian lower lithosphere is denser than the underlying mantle and will delaminate (Capitanio et al., 2010). The length of our proposed north-dipping subducting ICL is at a minimum ~550 km assumed to be a rigid body (Fig. 7, profile B–B'). If we assume that the ICL has maintained a constant convergence velocity with respect to Tibet (currently ~20 mm/yr) across the Himalayas based on GPS measurements (Bettinelli et al., 2006), we would estimate that the current stage of continental subduction started at least ~25–30 Ma ago.

Thus far our interpretation has ignored the HVBNL. It is possible that the HVBNL represents remnant Tibetan lithosphere associated with the late Precambrian basement of the Lhasa Block (Zhu et al., 2011), in which case its presence may have little bearing on the modern geometry or earlier evolution of the subducting ICL. However, if the HVBNL represents a separate piece of the ICL, then the ICL must have underthrust horizontally beneath Tibet nearly to the BNS at an earlier stage of continental collision to emplace the HVBNL (Fig. 9a), before the modern subduction geometry was established. In this scenario, the 170 km difference between the minimum length of the entire ICL on cross-section B–B' of Fig. 7a (~550 km) and the distance of the HVBNL from the MFT (~380 km) provides a minimum estimate for the initiation of delamination–subduction: ~10 Ma at a convergence rate of ~20 mm/yr. If, as widely believed (e.g., Chung et al., 2009), it was the onset of roll-back or delamination of underthrust ICL that triggered widespread post-collisional potassic volcanism across southern Tibet from ~25–10 Ma, then in the scenario of Fig. 9a the subducting ICL should now continue an additional ~300 km down-dip to a depth of ~600 km. These depths are below the limit of our study. However, a deeper high-velocity anomaly body has

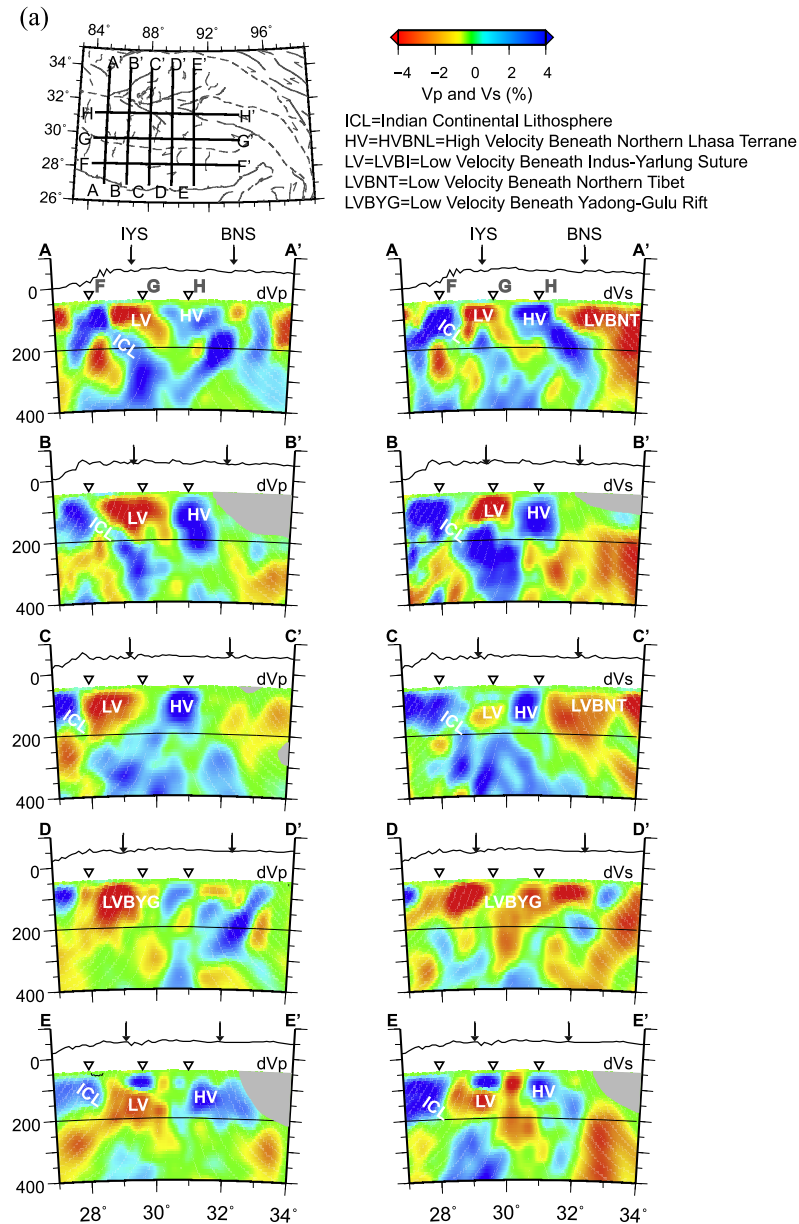


**Fig. 7.** (a) Five south–north and (b) three west–east vertical cross-sections through our P- and S-wave velocity models. Topography on the vertical sections is exaggerated  $\times 10$ . The top 50 km of the model has been removed because crustal structure is poorly constrained. Arrows above each section mark the IYS and BNS. Open inverted triangles show the intersection points of south–north and west–east cross-sections. Velocity anomalies are labeled as in Fig. 6. (For interpretation of the references to color in this figure legend, the reader is referred to the web version of this article.)

been observed in previous tomographic studies (Li et al., 2008). Possible lateral necking of the subducting ICL at a depth of about 180–220 km (Fig. 7a, e.g. B–B', C–C') could represent ongoing detachment of the ICL (Fig. 9a, bottom panel).

In contrast to A–A' and B–B' (Fig. 7a), which are suggestive of a subduction geometry of the down-going ICL, the anomalies present in cross-sections C–C' and E–E' appear more symmetric north and south of the LVBI. This pattern suggests the presence of a detachment of thickened ICL caused by Rayleigh–Taylor gravitational instability (Fig. 9b). In this scenario, the high-velocity anomalies at  $>200$  km depth beneath the IYS that correlate with the thickest crust ( $\sim 80$  km) in Tibet would represent detached ICL. When considering Rayleigh–Taylor instability, the total volume of the ICL should be conserved during local thickening. Assuming subduction of  $\sim 100$  km-thick Indian mantle lithosphere at a constant rate of  $\sim 20$  mm/yr, the input area per year along the B–B' profile will

be  $2.0 \times 10^{-3}$  km<sup>2</sup>/yr. The area of the gap between the ICL and HVBNL is  $\sim 1.6 \times 10^4$  km<sup>2</sup> and the area for the detached body is about  $4 \times 10^4$  km<sup>2</sup>. The difference between these two areas is  $\sim 2.4 \times 10^4$  km<sup>2</sup>, which would have taken  $\sim 12$  Ma to accumulate by underthrusting of ICL. This timing seems far too late to explain the potassic volcanics erupted from  $\sim 25$ –10 Ma (Chung et al., 2009). Unless an earlier episode of instability led to detachment of a similar sized body that is now below 400 km depth, a depth invisible to our tomography (e.g. as shown by DeCelles et al., 2002), it is hard to reconcile our tomographic results with a convective removal process that led to formation of the observed mantle melts.

The P-wave tomographic image of the upper mantle beneath central Tibet from INDEPTH III data (Tilmann et al., 2003) revealed a sub-vertical high-velocity zone from about 100 km to 400 km depth, south of the BNS, interpreted as “downwelling” (subducting

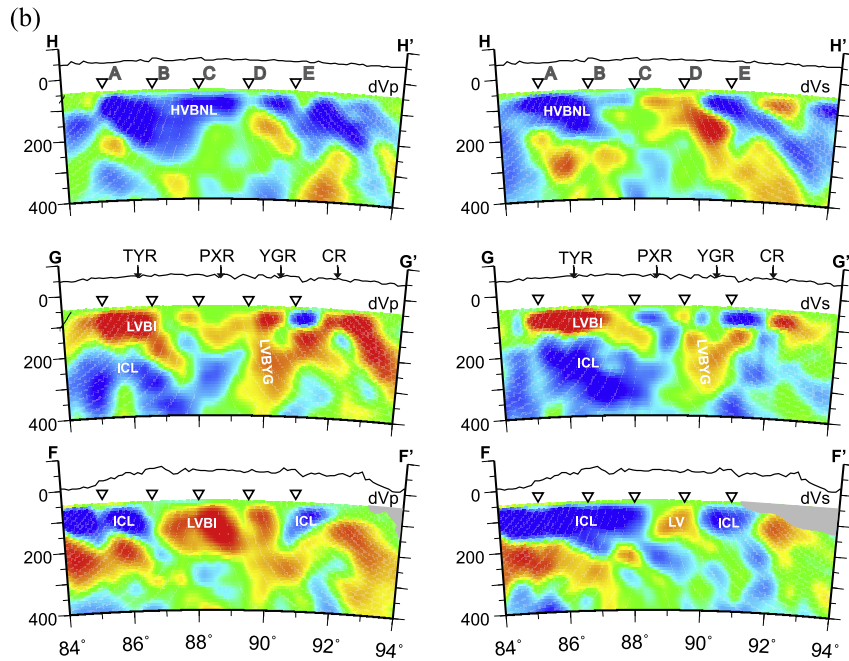


Fig. 7. (continued)

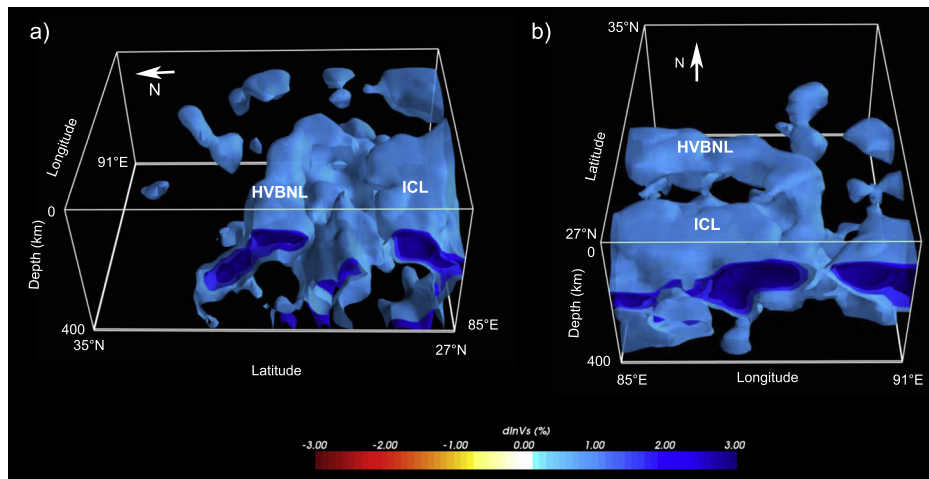


Fig. 8. 3D iso-surface plots for the S-wave model. (a) A west-east view and (b) a south-north view of the 3D S-wave model, labeled as in Fig. 6. The different blue iso-surfaces are showing 1%, 2%, 3% and 4% high-velocity anomalies, respectively. Low-velocity anomalies are not shown (see Fig. S4). (For interpretation of the references to color in this figure legend, the reader is referred to the web version of this article.)

or detaching) ICL. Our updated 3D images show a high-velocity body at a similar location (Fig. 7, profile D–D’, part of our HVBNL), but with less west-east lateral continuity than implicitly inferred by Tilmann et al. (2003) and disconnected from our proposed subducting ICL.

Our results show significant low-velocity anomalies in the upper mantle beneath southern Tibet (Figs. 6 and 7). One body is centered at 90°E and the other is centered at 94°E, which confirms the geometry and depth extent of the low P- and S-wave velocities found by previous regional finite-frequency tomography studies (Ren and Shen, 2008; Liang et al., 2011, 2012). Our results suggest that the current ICL is not uniformly distributed at depth and has significant orogen-parallel variations in both P- and S-wave velocities. The geometry of the ICL is likely more complex than suggested by simple interpretations of the 2D, approximately south-north, seismic profiles in southern Tibet.

### 5.2. Inherited lateral variations of Indian lithosphere

We cannot fully rule out the possibility that the upper-mantle low-velocity anomalies beneath southern Tibet are due to compositional variations within the ICL that either represent preserved Precambrian terrane boundaries or were formed during a Permo-Triassic rifting event (Liang et al., 2012). Surface wave tomography of the Dharwar Craton, south India, shows lateral inhomogeneity from 40–100 km depth up to ±2% over length scales of ~200 km (Borah et al., 2014). This amount of lateral inhomogeneity is enough to explain a significant part of our observed variations in velocity (Fig. 7). Caldwell et al. (2013) discuss along-strike changes in crustal thickness entering the Himalayan subduction zone of >10 km. Three ~south-north paleotopographic subsurface ridges mapped beneath the Gangetic foreland basin, and possibly beneath the Himalaya (Fig. 1) (Godin and Harris, 2014), probably also represent along-strike crustal differ-

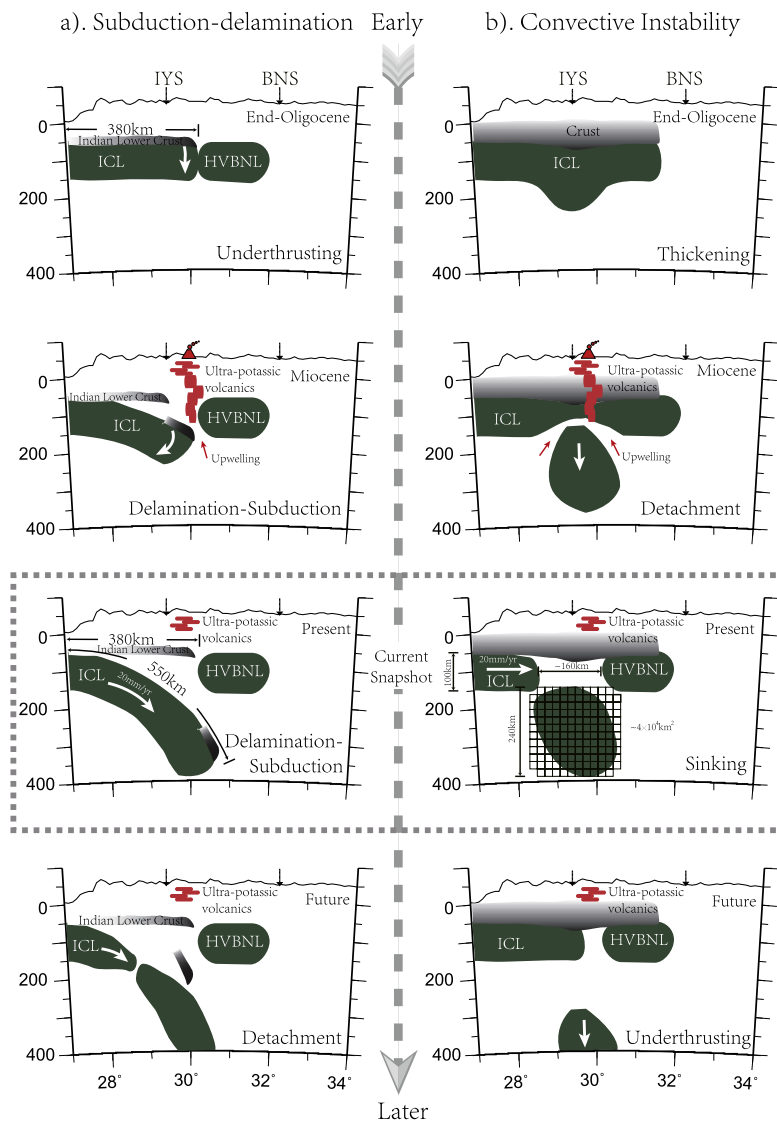


**Fig. 9.** Speculative models for the temporal evolution of upper mantle convergence between India and Tibet. The dashed rectangle encloses the current snapshot for both scenarios based on our tomographic images (Fig. 6, B–B'). Dark-green regions are continental mantle lithosphere. (a) Left panel: underthrusting Indian continental lithosphere rolls back to become a subducting slab. (b) Right panel: underthrusting Indian continental lithosphere is thickened during collision then later lost due to Rayleigh–Taylor instability. Each small square on the third plot (current snapshot) represents an area of 400 km<sup>2</sup>. (For interpretation of the references to color in this figure legend, the reader is referred to the web version of this article.)

ences. However, given the uncertainty as to how much of the Indian crust is subducted, it is unclear whether or not these along-strike changes directly contribute to our observed velocity perturbations. Given the likelihood that the ICL has undergone substantial deformation during subduction, we conclude that the low-velocity anomalies we observed beneath southern Tibet are most likely the consequence of recent fragmentation of the Indian lithosphere (Liang et al., 2012). The west–east variations of the Indian lithosphere could facilitate the fragmentation process (Godin and Harris, 2014), since concentrations of strain occurring at changes in lithospheric thickness or density could induce changes in subduction angle (Li et al., 2008; Chen et al., 2015) and trigger the proposed lithospheric tearing (Liang et al., 2012). We cannot distinguish this from other possible causes of lithospheric fragmentation, including the curvature of the Himalayan subduction front (McCaffrey and Nabelek, 1998), gravitational instability of the thickened ICL (Houseman and Molnar, 1997), and dynamics related to the subduction of the Indian plate beneath southeastern Tibet and Burma.

### 5.3. Possible link between west–east extension and the fragmentation of the ICL

Our low-velocity anomalies in the shallow mantle are spatially correlated with (from west to east) the Tangra Yum Co, Yadong-Gulu, and Cona Rifts (Fig. 1), down to depths of 100–150 km beneath the TYR and to ~400 km beneath the YGR and CR. The low-velocity anomaly near 90°E connects with the low-velocity anomalies beneath the IYS and north of the BNS, agreeing well with other images of alternating high and low velocities beneath southern Tibet (Liang and Song, 2006; Hearn et al., 2011; Wang et al., 2013). The N–S trending uppermost mantle low-velocity feature beneath the YGR is also observed in the Pn tomography images (Liang and Song, 2006). The Pn tomography image of Hearn et al. (2011) showed the west–east variability of Pn velocities beneath the Himalayas and southern Tibet, indicating that the subducted ICL is not a homogeneous body. These north–south trending low-velocity anomalies have previously been interpreted as evidence of fragmentation of the ICL (Liang et al., 2011, 2012),

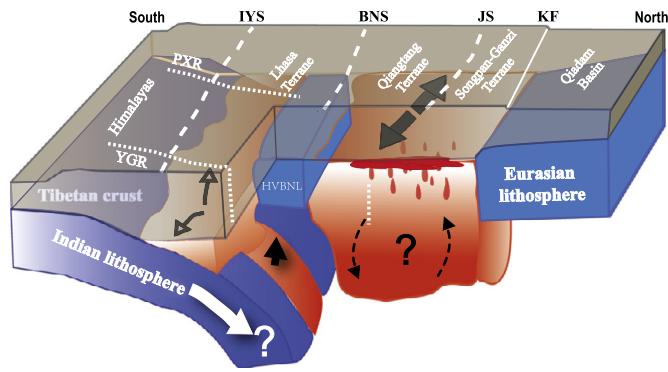


**Fig. 10.** Cartoon interpretation of the current upper-mantle structure beneath south-central Tibet. The fragmented ICL is helping to drive convection beneath northern Tibet. The lithospheric mantle of northern Tibet is heated by both viscous strain heating and small-scale mantle convection induced by the downwelling of the ICL. Upwelling asthenosphere through gaps in the ICL flows laterally above the subducting slab. Black arrows show the direction of mantle material flow. (For interpretation of the references to color in this figure legend, the reader is referred to the web version of this article.)

and may also act as channels for asthenospheric flow between the shallower low-velocity zone in southern Tibet and the much larger low-velocity zone in central-northern Tibet (Liang and Song, 2006).

It is debated whether Tibet's surface rifting extends through the whole lithosphere (Yin, 2000) or is limited to the upper crust (e.g., McCaffrey and Nabelek, 1998). Our upper-mantle low velocities do not spatially match the surface rifts one to one. Nonetheless, discrete asthenospheric upwellings could create a west–east basal shear on the Tibetan crust that stimulates surface rifting (Tian et al., 2015).

The extensional and strike-slip sub-Moho earthquakes (~80–95 km) in southern Tibet (de la Torre et al., 2007; Jiang et al., 2009) may reflect our inferred lithosphere fragmentation. However, if crustal extension is directly related to lithospheric fragmentation, the fragmentation should start at least as early as the surface rifting process, for which the oldest dates yet reported are 19 Ma (Mitsuishi et al., 2012). The earliest west–east extension yet known is a few million years younger than the initiation of the widespread potassic volcanism (~25 Ma) that may alternatively or additionally be related to lithospheric fragmentation.

## 6. Conclusions: an updated three-dimensional model for the Indian lithosphere

Using our updated finite-frequency body-wave tomography results in the south-central Tibetan Plateau, we update our 3D dynamic model of the Indian lithosphere from Liang et al. (2012) (Fig. 10). Indian continental lithosphere is currently subducting beneath southern Tibet. This lithosphere can be seen in our model as seismically faster, presumably colder material dipping northward at ~40°, reaching the BNS at a depth of 350 km. Beneath southern Tibet we observe alternating low- and high-velocity anomalies from west to east that we believe indicate lateral fragmentation of the ICL perpendicular to the India–Asia convergence direction between India and Eurasia. At the same time gravitational detachment of the subducted ICL may be developing along the strike of the collisional mantle front from east to west. We infer that fragmentation has induced local upwelling of asthenosphere beneath the subducting ICL, imaged as low-velocity anomalies that separate the strong fast-velocity anomalies of the subducting ICL. The most significant low-velocity anomaly, i.e. our largest proposed tear, is west of the YGR, extending far to the north and connecting with the low-velocity anomaly beneath the Qiangtang Terrane. Indian asthenosphere may be ascending west of the YGR and flowing northward to mix with asthenosphere beneath northern Tibet.

Establishing 3D images of the subducting ICL is an essential step towards a full understanding of the Indian–Eurasian continental collision and the construction of the Tibetan Plateau. Detailed surface-wave tomography using similar data sets will provide a solid test of our 3D model of the upper-mantle structure of the south-central Tibetan Plateau, while joint inversion of body- and surface-wave tomography will further improve the details of the 3D velocity architecture.

## Acknowledgements

We express our appreciation of Professor Zhongjie Zhang, who died on September 6th, 2013. Without his efforts, inspiring ideas, and continuous encouragement this research would neither have begun nor been finished. We thank our colleagues and Tibetan drivers for their help in the field during TIBET-31N. Seismic Array Laboratory, IGGCAS, provided instruments and maintenance for TIBET-31N. Min Chen helped make the 3D iso-surface plots. She also provided valuable comments along with Mian Liu. Discussions with Chuan-Zhou Liu and Fu-Yuan Wu helped our interpretation. Xiaofeng Liang benefits from the discussions in Coffice 442 of IGGCAS. Constructive comments by two anonymous reviewers also helped to improve the manuscript. IRIS DMC and the INDEPTH, HIMNT, BHUTAN, Namche Barwa, Hi-CLIMB, RISE experiments made the seismic data available. Generic Mapping Tools (GMT) was used to produce most of the figures in this study. Mayavi was used to make the 3D iso-surface plots and Seismic Analysis Code (SAC) was used for data processing. This research is supported by the Strategic Priority Research Program (B) of the Chinese Academy of Sciences (grant XDB03010700), Sinoprobe-02-03, and National Natural Science Foundation of China (grants 41404051, 41274066, 41374063, 41274090 and 41574056). This work is also supported by NSF grant EAR-0409870 to New Mexico State University.

## Appendix A. Supplementary material

Supplementary material related to this article can be found online at <http://dx.doi.org/10.1016/j.epsl.2016.03.029>.

## References

- Acton, C.E., Priestley, K., Gaur, V.K., Rai, S.S., 2010. Group velocity tomography of the Indo-Eurasian collision zone. *J. Geophys. Res.* 115, B12335.
- Agius, M.R., Lebedev, S., 2013. Tibetan and Indian lithospheres in the upper mantle beneath Tibet: evidence from broadband surface-wave dispersion. *Geochem. Geophys. Geosyst.* 14, 4260–4281.
- Argand, E., 1924. La tectonique de l'Asie. In: 13th Int. Geol. Congr. Rep. Sess., vol. 1(5), pp. 171–372.
- Armijo, R., Tapponnier, P., Mercier, J., Tong-Lin, H., 1986. Quaternary extension in southern Tibet: field observations and tectonic implications. *J. Geophys. Res.* 91, 13803–13872.
- Bao, X., Song, X., Li, J., 2015. High-resolution lithospheric structure beneath Mainland China from ambient noise and earthquake surface-wave tomography. *Earth Planet. Sci. Lett.* 417, 132–141.
- Barron, J., Priestley, K., 2009. Observations of frequency-dependent Sn propagation in Northern Tibet. *Geophys. J. Int.* 179, 475–488.
- Bassin, C., Laske, G., Masters, G., 2000. The current limits of resolution for surface wave tomography in North America. *Eos Trans. AGU* 81, 897.
- Bettinelli, P., Avouac, J.-P., Flouzat, M., Jouanne, F., Bollinger, L., Willis, P., Chitrakar, G., 2006. Plate motion of India and interseismic strain in the Nepal Himalaya from GPS and DORIS measurements. *J. Geod.* 80, 567–589.
- Borah, K., Rai, S.S., Priestley, K., Gaur, V.K., 2014. Complex shallow mantle beneath the Dharwar Craton inferred from Rayleigh wave inversion. *Geophys. J. Int.* 198, 1055–1070.
- Caldwell, W.B., Klemperer, S.L., Lawrence, J.F., Rai, S.S., Ashish, 2013. Characterizing the Main Himalayan Thrust in the Garhwal Himalaya, India with receiver function CCP stacking. *Earth Planet. Sci. Lett.* 367, 15–27.
- Capitanio, F.A., Morra, G., Goes, S., Weinberg, R.F., Moresi, L., 2010. India–Asia convergence driven by the subduction of the Greater Indian continent. *Nat. Geosci.* 3, 136–139.

- Ceylan, S., Ni, J., Chen, J.Y., Zhang, Q., Tilmann, F., Sandvol, E., 2012. Fragmented Indian plate and vertically coherent deformation beneath eastern Tibet. *J. Geophys. Res.* 117, B11303.
- Chen, W.-P., Martin, M., Tseng, T.-L., Nowack, R.L., Hung, S.-H., Huang, B.-S., 2010a. Shear-wave birefringence and current configuration of converging lithosphere under Tibet. *Earth Planet. Sci. Lett.* 295, 297–304.
- Chen, Y., Badal, J., Hu, J., 2010b. Love and Rayleigh wave tomography of the Qinghai-Tibet Plateau and surrounding areas. *Pure Appl. Geophys.* 167, 1171–1203.
- Chen, Y., Li, W., Yuan, X., Badal, J., Teng, J., 2015. Tearing of the Indian lithospheric slab beneath southern Tibet revealed by SKS-wave splitting measurements. *Earth Planet. Sci. Lett.* 413, 13–24.
- Chung, S.-L., Chu, M.-F., Ji, J., O'Reilly, S.Y., Pearson, N.J., Liu, D., Lee, T.-Y., Lo, C.-H., 2009. The nature and timing of crustal thickening in southern Tibet: geochemical and zircon Hf isotopic constraints from postcollisional adakites. *Tectonophysics* 477, 36–48.
- Dahlen, F.A., Hung, S.-H., Nolet, G., 2000. Fréchet kernels for finite-frequency travel-times – I: theory. *Geophys. J. Int.* 141, 157–174.
- de la Torre, T.L., Monsalve, G., Sheehan, A.F., Sapkota, S., Wu, F., 2007. Earthquake processes of the Himalayan collision zone in eastern Nepal and the southern Tibetan Plateau. *Geophys. J. Int.* 171, 718–738.
- DeCelles, P.G., Robinson, D.M., Zandt, G., 2002. Implications of shortening in the Himalayan fold-thrust belt for uplift of the Tibetan Plateau. *Tectonics* 21, 1062.
- Dewey, J.F., Burke, K.C.A., 1973. Tibetan, Variscan, and Precambrian basement reactivation: products of continental collision. *J. Geol.* 81, 683–692.
- England, P., Houseman, G., 1986. Finite strain calculations of continental deformation. 2: comparison with the India-Asia collision zone. *J. Geophys. Res.* 91, 3664–3676.
- Fu, Y.V., Chen, Y.J., Li, A., Zhou, S., Liang, X., Ye, G., Jin, G., Jiang, M., Ning, J., 2008. Indian mantle corner flow at southern Tibet revealed by shear wave splitting measurements. *Geophys. Res. Lett.* 35, L02308.
- Fu, Y.V., Li, A., Chen, Y.J., 2010. Crustal and upper mantle structure of southeast Tibet from Rayleigh wave tomography. *J. Geophys. Res.* 115, B12323.
- Godin, L., Harris, L.B., 2014. Tracking basement cross-strike discontinuities in the Indian crust beneath the Himalayan orogen using gravity data – relationship to upper crustal faults. *Geophys. J. Int.* 198, 198–215.
- He, R., Zhao, D., Gao, R., Zheng, H., 2010. Tracing the Indian lithospheric mantle beneath central Tibetan Plateau using teleseismic tomography. *Tectonophysics* 491, 230–243.
- Hearn, T.M., Wang, H., Chen, Y.J., Sandvol, E.A., Ni, J.F., 2011. Three-dimensional variations in the Tibetan mantle lid velocity from Pn tomography. In: AGU Fall Meeting. San Francisco. pp. T43A-2293.
- Houseman, G.A., Molnar, P., 1997. Gravitational (Rayleigh-Taylor) instability of a layer with non-linear viscosity and convective thinning of continental lithosphere. *Geophys. J. Int.* 128, 125–150.
- Huang, W.C., Ni, J.F., Tilmann, F., Nelson, D., Guo, J., Zhao, W., Mechie, J., Kind, R., Saul, J., Rapine, R., Hearn, T.M., 2000. Seismic polarization anisotropy beneath the central Tibetan Plateau. *J. Geophys. Res.* 105, 27979–27989.
- Hung, S.-H., Chen, W.-P., Chiao, L.-Y., 2011. A data-adaptive, multiscale approach of finite-frequency, traveltimes tomography with special reference to P and S wave data from central Tibet. *J. Geophys. Res.* 116, B06307.
- Jiang, M.M., Zhou, S.Y., Tong, X.P., Liang, X.F., Chen, Y.-S., 2009. Accurate depth determination of deep earthquake in southern Tibet and its geodynamic implication. *Chin. J. Geophys.* 52, 2237–2244 (in Chinese).
- Jiang, M., Zhou, S., Sandvol, E., Chen, X., Liang, X., Chen, Y.J., Fan, W., 2011. 3-D lithospheric structure beneath southern Tibet from Rayleigh-wave tomography with a 2-D seismic array. *Geophys. J. Int.* 185, 593–608.
- Jin, G., Chen, Y., Basang, C., 2009. Investigation of local earthquakes in the Lhasa region. *Chin. J. Geophys.* 52, 3020–3026 (in Chinese).
- Jin, Y., McNutt, M.K., Zhu, Y., 1996. Mapping the descent of Indian and Eurasian plates beneath the Tibetan Plateau from gravity anomalies. *J. Geophys. Res.* 101, 11275–11290.
- Kind, R., Yuan, X., Saul, J., Nelson, D., Sobolev, S.V., Mechie, J., Zhao, W., Kosarev, G., Ni, J., Achauer, U., Jiang, M., 2002. Seismic images of crust and upper mantle beneath Tibet: evidence for Eurasian plate subduction. *Science* 298, 1219–1221.
- Kosarev, G., Kind, R., Sobolev, S.V., Yuan, X., Hanka, W., Oreshin, S., 1999. Seismic evidence for a detached India lithospheric mantle beneath Tibet. *Science* 283, 1306–1309.
- Kumar, P., Yuan, X., Kind, R., Ni, J., 2006. Imaging the colliding Indian and Asian lithospheric plates beneath Tibet. *J. Geophys. Res.* 111, B06308.
- Laske, G., Masters, G., Ma, Z., Pasyanos, M., 2013. Update on CRUST1.0 – a 1-degree global model of Earth's crust. *Geophys. Res. Abstr.* 15, Abstract EGU2013-2658.
- Li, C., Hilst, R.D.V.D., Meltzer, A.S., Engdahl, E.R., 2008. Subduction of the Indian lithosphere beneath the Tibetan Plateau and Burma. *Earth Planet. Sci. Lett.* 274, 157–168.
- Liang, X., Shen, Y., Chen, Y.J., Ren, Y., 2011. Crustal and mantle velocity models of southern Tibet from finite frequency tomography. *J. Geophys. Res.* 116, B02408.
- Liang, X., Sandvol, E., Chen, Y.J., Hearn, T., Ni, J., Klemperer, S., Shen, Y., Tilmann, F., 2012. A complex Tibetan upper mantle: a fragmented Indian slab and no south-verging subduction of Eurasian lithosphere. *Earth Planet. Sci. Lett.* 333–334, 101–111.
- Liang, C., Song, X., 2006. A low velocity belt beneath northern and eastern Tibetan Plateau from Pn tomography. *Geophys. Res. Lett.* 33, L22306.
- Liu, M., Yang, Y., 2003. Extensional collapse of the Tibetan Plateau: results of three-dimensional finite element modeling. *J. Geophys. Res.* 108, 2361.
- Lou, X., van der Lee, S., Lloyd, S., 2013. AIMBAT: a Python/Matplotlib tool for measuring teleseismic arrival times. *Seismol. Res. Lett.* 84, 85–93.
- Masek, J.G., Isacks, B.L., Fielding, E.J., Browaeys, J., 1994. Rift flank uplift in Tibet: evidence for a viscous lower crust. *Tectonics* 13, 659–667.
- McCaffrey, R., Nabelek, J., 1998. Role of oblique convergence in the active deformation of the Himalayas and southern Tibet plateau. *Geology* 26, 691–694.
- McNamara, D.E., Owens, T.J., Walter, W.R., 1995. Observations of regional phase propagation across the Tibetan Plateau. *J. Geophys. Res.* 100, 22215–22229.
- Mitsuishi, M., Wallis, S.R., Aoya, M., Lee, J., Wang, Y., 2012. E-W extension at 19 Ma in the Kung Co area, S. Tibet: evidence for contemporaneous E-W and N-S extension in the Himalayan orogen. *Earth Planet. Sci. Lett.* 325–326, 10–20.
- Molnar, P., Tapponnier, P., 1978. Active tectonics of Tibet. *J. Geophys. Res.* 83, 5361–5375.
- Molnar, P., Tapponnier, P., Chen, W.P., 1981. Extensional tectonics in central and eastern Asia – a brief summary. *Philos. Trans. R. Soc. Lond. A* 300, 403–406.
- Molnar, P., England, P., Martinod, J., 1993. Mantle dynamics, uplift of the Tibetan Plateau, and the Indian Monsoon. *Rev. Geophys.* 31, 357–396.
- Nabelek, J., Hetenyi, G., Vergne, J., Sapkota, S., Kafle, B., Jiang, M., Su, H.P., Chen, J., Huang, B.S., Team, H.-C., 2009. Underplating in the Himalaya-Tibet collision zone revealed by the Hi-CLIMB experiment. *Science* 325, 1371–1374.
- Ni, J., Barazangi, M., 1983. High-frequency seismic wave propagation beneath the Indian Shield, Himalayan Arc, Tibetan Plateau and surrounding regions: high uppermost mantle velocities and efficient Sn propagation beneath Tibet. *Geophys. J. R. Astron. Soc.* 72, 665–689.
- Ni, J., Barazangi, M., 1984. Seismotectonics of the Himalayan collision zone: geometry of the underthrusting Indian Plate beneath the Himalaya. *J. Geophys. Res.* 89, 1147–1163.
- Ni, J., York, J.E., 1978. Late cenozoic tectonics of the Tibetan Plateau. *J. Geophys. Res.* 83, 5377–5384.
- Nunn, C., Roecker, S.W., Priestley, K.F., Liang, X., Gilligan, A., 2014. Joint inversion of surface waves and teleseismic body waves across the Tibetan collision zone: the fate of subducted Indian lithosphere. *Geophys. J. Int.* 198, 1526–1542.
- Owens, T.J., Zandt, G., 1997. Implications of crustal property variations for models of Tibetan plateau evolution. *Nature* 387, 37–43.
- Pavlis, G.L., Vernon, F.L., 2010. Array processing of teleseismic body waves with the USArray. *Comput. Geosci.* 36, 910–920.
- Priestley, K., Jackson, J., McKenzie, D., 2008. Lithospheric structure and deep earthquakes beneath India, the Himalaya and southern Tibet. *Geophys. J. Int.* 172, 345–362.
- Ren, Y., Shen, Y., 2008. Finite frequency tomography in southeastern Tibet: evidence for the causal relationship between mantle lithosphere delamination and the north-south trending rifts. *J. Geophys. Res.* 113, B10316.
- Royden, L.H., Burchfiel, B.C., King, R.W., Wang, E., Chen, Z.L., Shen, F., Liu, Y.P., 1997. Surface deformation and lower crustal flow in eastern Tibet. *Science* 276, 788–790.
- Schulte-Pelkum, V., Monsalve, G., Sheehan, A., Pandey, M.R., Sapkota, S., Bilham, R., Wu, F., 2005. Imaging the Indian subcontinent beneath the Himalaya. *Nature* 435, 1222–1225.
- Shi, D., Wu, Z., Klemperer, S.L., Zhao, W., Xue, G., Su, H., 2015. Receiver function imaging of crustal suture, steep subduction, and mantle wedge in the eastern India-Tibet continental collision zone. *Earth Planet. Sci. Lett.* 414, 6–15.
- Sol, S., Meltzer, A., Burgmann, R., Hilst, R.D.V.D., King, R., Chen, Z., Koons, P.O., Lev, E., Liu, Y.P., Zeitler, P.K., Zhang, X., Zhang, J., Zurek, B., 2007. Geodynamics of the southern Tibetan Plateau from seismic anisotropy and geodesy. *Geology* 35, 563–566.
- Styron, R., Taylor, M., Okoronkwo, K., 2010. Database of active structures from the Indo-Asian collision. *Eos Trans. AGU* 91, 181–182.
- Sun, Y., Li, X., Kuleli, S., Morgan, F.D., Toksoz, M.N., Wang, Q., Zhang, P., Freymueller, J.T., Bilham, R., Larson, K.M., Lai, X., You, X., Niu, Z., Wu, J., Li, Y., Liu, J., Yang, Z., Chen, Q., 2004. Adaptive moving window method for 3D P-velocity tomography and its application in China. *Bull. Seismol. Soc. Am.* 94, 740–746.
- Sun, Y., Toksoz, M.N., Pei, S., Morgan, F.D., 2008. The layered shear-wave velocity structure of the crust and uppermost mantle in China. *Bull. Seismol. Soc. Am.* 98, 746–755.
- Tian, X., Chen, Y., Tseng, T.-L., Klemperer, S.L., Thybo, H., Liu, Z., Xu, T., Liang, X., Bai, Z., Zhang, X., Si, S., Sun, C., Lan, H., Wang, E., Teng, J., 2015. Weakly coupled lithospheric extension in southern Tibet. *Earth Planet. Sci. Lett.* 430, 171–177.
- Tilmann, F., Ni, J., INDEPTH Seismic Team, 2003. Seismic imaging of the downwelling Indian lithosphere beneath central Tibet. *Science* 300, 1424–1427.
- VanDecar, J.C., Crosson, R.S., 1990. Determination of teleseismic relative phase arrival times using multi-channel cross-correlation and least squares. *Bull. Seismol. Soc. Am.* 80, 150–169.
- Velasco, A.A., Gee, V.L., Rowe, C., Grujic, D., Hollister, L.S., Hernandez, D., Miller, K.C., Tobgay, T., Fort, M., Harder, S., 2007. Using small, temporary seismic networks for investigating tectonic deformation: brittle deformation and evidence from

- strike-slip faulting in Bhutan. *Seismol. Res. Lett.* 78, 446–453.
- Wang, H., Hearn, T., Chen, Y., Pei, S., Feng, Y., Yue, H., Jin, G., Zhou, S., Wang, Y., Ge, Z., Ning, J., Sandvol, E., Ni, J., 2013. Pn wave tomography of eastern Tibetan plateau. *Chin. J. Geophys.* 56, 472–480 (in Chinese).
- Wittlinger, G., Masson, F., Poupinet, G., Tapponnier, P., Jiang, M., Herquel, G., Guilbert, J., Achauer, U., Xue, G., Shi, D., Team, L.K., 1996. Seismic tomography of northern Tibet and Kunlun: evidence for crustal blocks and mantle velocity contrasts. *Earth Planet. Sci. Lett.* 139, 263–279.
- Yang, T., Shen, Y., 2006. Frequency-dependent crustal correction for finite-frequency seismic tomography. *Bull. Seismol. Soc. Am.* 96, 2441–2448.
- Yin, A., 2000. Mode of Cenozoic east–west extension in Tibet suggesting a common origin of rifts in Asia during the Indo-Asian collision. *J. Geophys. Res.* 105, 21745–21759.
- Zhang, Z., Chen, Y., Yuan, X., Tian, X., Klempner, S.L., Xu, T., Bai, Z., Zhang, H., Wu, J., Teng, J., 2013. Normal faulting from simple shear rifting in South Tibet, using evidence from passive seismic profiling across the Yadong-Gulu Rift. *Tectonophysics* 606, 178–186.
- Zhang, X., Teng, J., Sun, R., Romanelli, F., Zhang, Z., Panza, G.F., 2014a. Structural model of the lithosphere–asthenosphere system beneath the Qinghai–Tibet Plateau and its adjacent areas. *Tectonophysics* 634, 208–226.
- Zhang, Z., Wang, Y., Houseman, G.A., Xu, T., Wu, Z., Yuan, X., Chen, Y., Tian, X., Bai, Z., Teng, J., 2014b. The Moho beneath western Tibet: shear zones and eclogitization in the lower crust. *Earth Planet. Sci. Lett.* 408, 370–377.
- Zhang, H., Zhao, D., Zhao, J., Liu, H., 2015. Tomographic imaging of the underthrusting Indian slab and mantle upwelling beneath central Tibet. *Gondwana Res.* 28, 121–132.
- Zhao, W.-L., Morgan, W.J., 1987. Injection of Indian crust into Tibetan lower crust: a two-dimensional finite element model study. *Tectonics* 6, 489–504.
- Zhao, J., Yuan, X., Liu, H., Kumar, P., Pei, S., Kind, R., Zhang, Z., Teng, J., Ding, L., Gao, X., Xu, Q., Wang, W., 2010. The boundary between the Indian and Asian tectonic plates below Tibet. *Proc. Natl. Acad. Sci.* 107, 11229–11233.
- Zhao, J., Murodov, D., Huang, Y., Sun, Y., Pei, S., Liu, H., Zhang, H., Fu, Y., Wang, W., Cheng, H., Tang, W., 2014. Upper mantle deformation beneath central-southern Tibet revealed by shear wave splitting measurements. *Tectonophysics* 627, 135–140.
- Zhou, H.W., Murphy, M.A., 2005. Tomographic evidence for wholesale underthrusting of India beneath the entire Tibetan plateau. *J. Asian Earth Sci.* 25, 445–457.
- Zhu, D.-C., Zhao, Z.-D., Niu, Y., Mo, X.-X., Chung, S.-L., Hou, Z.-Q., Wang, L.-Q., Wu, F.-Y., 2011. The Lhasa Terrane: record of a microcontinent and its histories of drift and growth. *Earth Planet. Sci. Lett.* 301, 241–255.